How to cite: *Angew. Chem. Int. Ed.* **2024**, *63*, e202401949
doi.org/10.1002/anie.202401949

X-Ray Scintillators

Overcoming Thermal Quenching in X-ray Scintillators through Multi-Excited State Switching

Min Wang, Zhongbo Zhang, Jing Lyu, Jian Qiu, Chang Gu, He Zhao, Tao Wang, Yiwen Ren, Shuo-Wang Yang, Guo Qin Xu, and Xiaogang Liu**

Abstract: X-ray scintillators have gained significant attention in medical diagnostics and industrial applications. Despite their widespread utility, scintillator development faces a significant hurdle when exposed to elevated temperatures, as it usually results in reduced scintillation efficiency and diminished luminescence output. Here we report a molecular design strategy based on a hybrid perovskite ($TpyBiCl_5$) that overcomes thermal quenching through multi-excited state switching. The structure of perovskite provides a platform to modulate the luminescence centers. The rigid framework constructed by this perovskite structure stabilized its triplet states, resulting in $TpyBiCl_5$ exhibiting an approximately 12 times higher (45 % vs. 3.8 %) photoluminescence quantum yield of room temperature phosphorescence than that of its organic ligand (Tpy). Most importantly, the interactions between the components of this perovskite enable the mixing of different excited states, which has been revealed by experimental and theoretical investigations. The $TpyBiCl_5$ scintillator exhibits a detection limit of 38.92 $nGy\,s^{-1}$ at 213 K and a detection limit of 196.31 $nGy\,s^{-1}$ at 353 K through scintillation mode switching between thermally activated delayed fluorescence and phosphorescence. This work opens up the possibility of solving the thermal quenching in X-ray scintillators by tuning different excited states.

X-ray scintillators have great utility in converting X-ray photons into visible light for imaging and detection purposes.[1] Despite their advantages in medical diagnostics and industrial applications, developing scintillators with highly sensitive performance at elevated temperatures remains a formidable challenge.[2] This is because of the decreased scintillation performance and diminished luminescent output caused by increased nonradiative processes. Inspired by ratiometric luminescence (dual emission) response to temperature, this implies that the material with temperature-responsive multi-emissions may provide a solution to solve this issue.[3] In general, organic molecules with abundant and adjustable energy levels offer a platform to generate muti-excited states, as a consequent, multi-emissions.[4] Recently, organic X-ray scintillators with thermally activated delayed fluorescence (TADF) or phosphorescence have gained attention for their ability to harness radiation-induced triplet excitons.[5] In particular, TADF and phosphorescence can be dynamically tuned by changing temperature.[6] Therefore, developing materials that exhibit simultaneous TADF and phosphorescence as well as good scintillation performance is a promising avenue of research for mitigating thermal quenching in this area.

We propose using organic–inorganic hybrid perovskites as a feasible solution. Hybrid perovskites are high-performance semiconductors with considerable thermal stability and reduced nonradiative decay due to the rigid framework constructed by alternate organic and inorganic

[*] Dr. M. Wang, Dr. J. Lyu, J. Qiu, C. Gu, H. Zhao, Dr. T. Wang, Prof. G. Qin Xu, Prof. X. Liu
Department of Chemistry
National University of Singapore
117543 Singapore, Singapore
E-mail: chmxugq@nus.edu.sg
chmlx@nus.edu.sg

Dr. Z. Zhang
School of Chemistry, Chemical Engineering and Biotechnology
Nanyang Technological University
637459 Singapore, Singapore

J. Qiu, C. Gu, H. Zhao, Prof. X. Liu
International Campus of Tianjin University
Joint School of National University of Singapore and Tianjin University
350207 Fuzhou, China

Y. Ren
Institute of Landscape Architecture
Zhejiang University
310058 Hangzhou, China

Prof. S.-W. Yang
Institute of High-Performance Computing, Agency for Science, Technology and Research
138632 Singapore, Singapore

Prof. G. Qin Xu, Prof. X. Liu
Center for Functional Materials
National University of Singapore Suzhou Research Institute
215123 Suzhou, China
E-mail: chmxugq@nus.edu.sg
chmlx@nus.edu.sg

components.[7] We hypothesize that hybrid perovskites can achieve multiple luminescent centers with TADF originating from the charge-transfer state between organic and inorganic components, and phosphorescence arising from localized triplet excited states in the organic part. The electronic coupling between the components can regulate the energy gap (ΔE_{ST}) between singlet (S_1) and triplet (T_1) states, allowing for the mixing of different excited states.[4c,8] Moreover, heavy atoms within the inorganic component not only boost X-ray absorptivity but also possess the ability to modulate intersystem crossing (ISC) and thermally activated reverse ISC.[5b,9]

To validate our hypothesis, we synthesized a zero-dimension hybrid perovskite based on $TpyBiCl_5$, using terpyridine (Tpy) and bismuth halide ($BiCl_3$) as organic and inorganic components, respectively. The terpyridine's low T_1 energy (435.5 nm in solution) is expected to generate phosphorescence in hybrid perovskites, further enhanced by interactions with the inorganic component (Figure 1).[10] $TpyBiCl_5$ exhibits simultaneous trimodal emission: prompt fluorescence, TADF, and phosphorescence at ambient conditions. The rigid structure of hybrid perovskites stabilizes the triplet excitons of terpyridine, leading to an increased room-temperature phosphorescence quantum yield from 3.8 % to 45.0 %. We examined the temperature-responsive X-ray scintillation of $TpyBiCl_5$, observing switchable TADF and phosphorescence emissions with changing temperatures. The detection limit improves from 73.04 $nGy\,s^{-1}$ at room temperature to 38.92 $nGy\,s^{-1}$ at 213 K, and remains at 196.31 $nGy\,s^{-1}$ at 353 K. These results demonstrate the possibility of developing multi-state emitting hybrid perovskites to address the thermal quenching in scintillators.

$TpyBiCl_5$ was synthesized using a solution-based hydrothermal reaction by dissolving Tpy and $BiCl_3$ in hydrochloric acid at a 1:1 ratio. The crystal structure of $TpyBiCl_5$ was characterized using single-crystal X-ray diffraction, revealing a triclinic system with space group P-1 (Table S1). The crystal structure consists of a typical zero-dimension structure at the molecular level, with isolated metal halides $[Bi_2Cl_{10}]^{4-}$ surrounded by protonated Tpy cations (Figure 2a and Figure S1), and its long-range order is driven by π–π stacking and hydrogen bonding interactions (Figure S2). In addition, the detailed structure and stability of as-synthe-

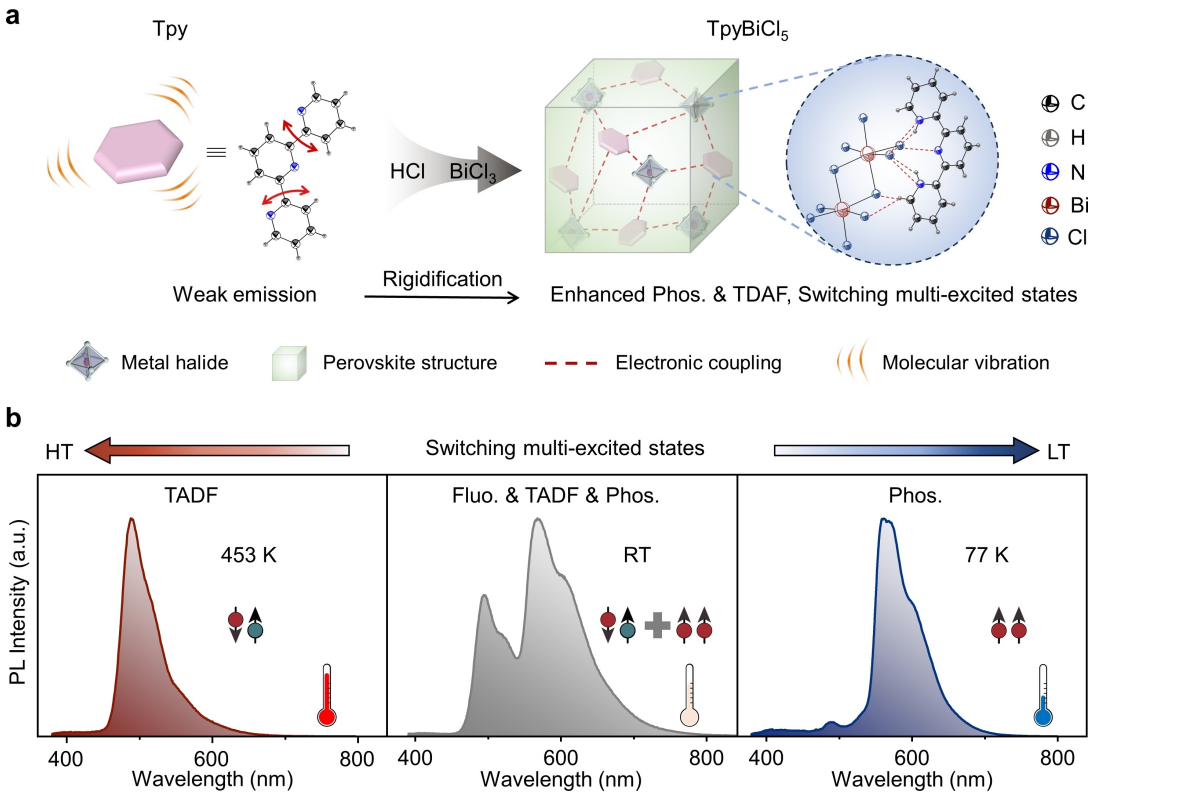

Figure 1. (a) Design principle of the hybrid perovskite with multiple excited states. Terpyridine (Tpy) with room temperature phosphorescence is chosen as the organic component of the hybrid perovskite and $BiCl_3$ as the inorganic component. The synthesized hybrid perovskite $TpyBiCl_5$ creates a rigid environment that suppresses the non-radiative relaxation of triplet excitons, evidenced by an increase in room-temperature phosphorescence quantum yield. In addition, the electronic coupling between the organic and inorganic parts of the hybrid perovskite enables charge transfer between them, allowing $TpyBiCl_5$ to simultaneously possess thermally activated delayed fluorescence characteristics, in addition to prompt fluorescence and phosphorescence. Room temperature, low temperature, and high temperature are abbreviated as RT, LT and HT, respectively. (b) Photoluminescence (PL) spectra of the hybrid perovskite ($TpyBiCl_5$) at high temperature (453 K), room temperature and low temperature (77 K), respectively. The TADF and phosphorescence have a separate emission band as Tpy has a lower triplet state. The dynamic switching between these excited states, which is triggered by the temperature, can mitigate thermal quenching in scintillators.

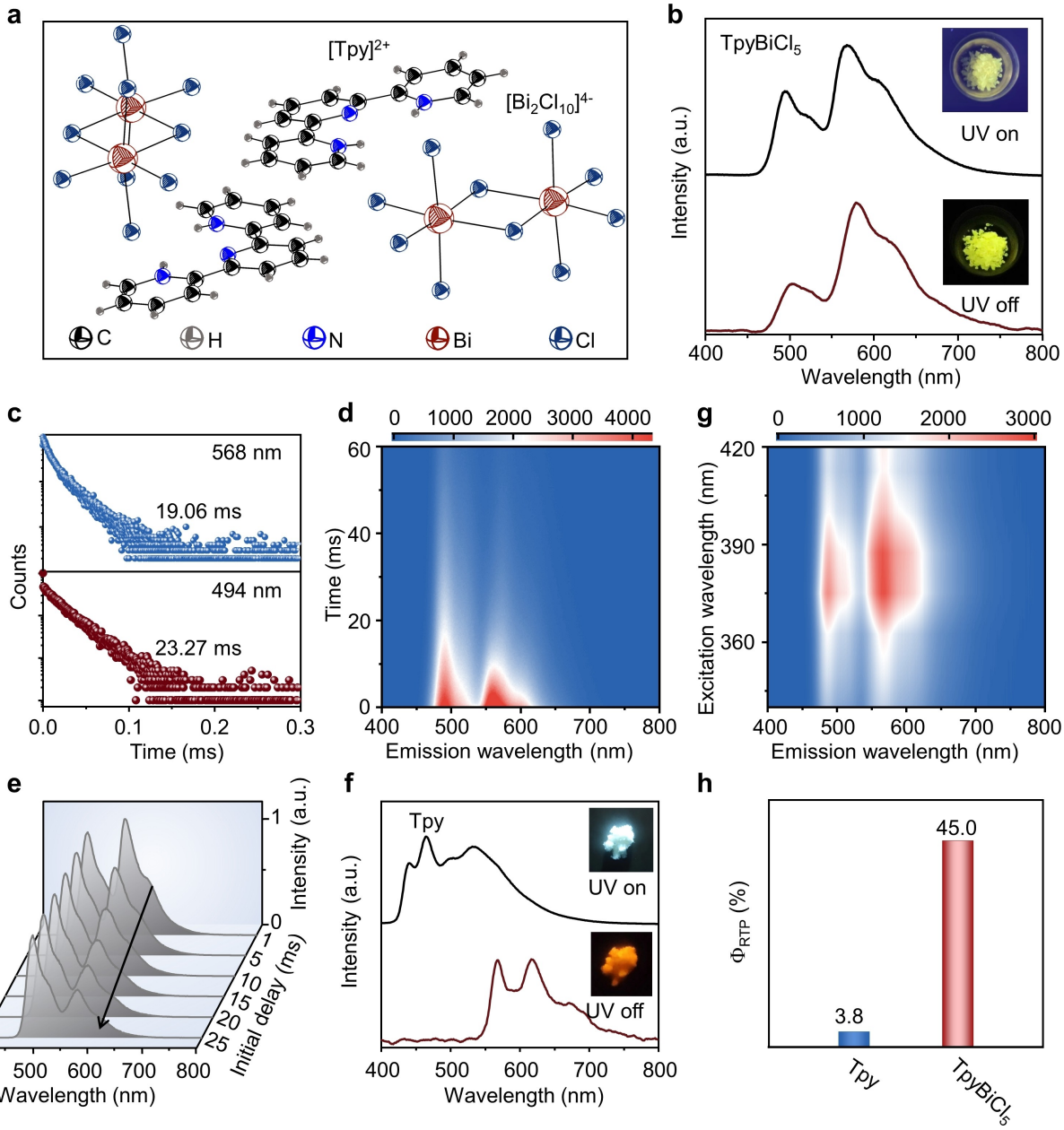

Figure 2. (a) Single crystal structure of $TpyBiCl_5$. This crystal arrangement belongs to a triclinic system with space group P-1, in which the isolated metal halides $[Bi_2Cl_{10}]^{4-}$ and the surrounding $[Tpy]^{2+}$ cations form the zero-dimensional structure at the molecular level. (b) Steady-state PL (black) and time-gated PL spectra (red) of $TpyBiCl_5$ ($\lambda_{ex}=360$ nm). Inset: photographs of $TpyBiCl_5$ taken before and after turning off the ultraviolet lamp (395 nm). (c) Lifetime decay profiles of the emission bands at 490 nm (red) and 568 nm (blue) of $TpyBiCl_5$ under excitation at 360 nm. (d) Time-resolved PL mapping of $TpyBiCl_5$ ($\lambda_{ex}=360$ nm). The color change from red to blue indicates the decrease in emission intensity. (e) Time-gated PL spectra of $TpyBiCl_5$ were recorded at different delay times and a gate of 5 ms. (f) Steady-state PL (black) and time-gated PL spectra (red) of Tpy ($\lambda_{ex}=360$ nm). Inset: photographs of Tpy taken before and after turning off the ultraviolet lamp (395 nm). (g) Excitation-delayed PL mapping of $TpyBiCl_5$. No shift in the phosphorescence peak was observed when the excitation wavelength was changed from 340 nm to 420 nm, indicating that no other impurities contribute to the phosphorescence of $TpyBiCl_5$. (h) Room-temperature phosphorescence quantum yield of Tpy and $TpyBiCl_5$ at ambient conditions ($\lambda_{ex}=360$ nm).

sized hybrid perovskites were characterized by nuclear magnetic resonance spectroscopy, Fourier transform infrared spectroscopy, powder X-ray diffraction, and thermal gravimetric analysis (Figure S3–9).

Under UV light excitation, the crystals emit a bright yellow-green light that persists as an afterglow after the excitation is turned off (Figure S10). The steady-state photoluminescence (PL) spectra of $TpyBiCl_5$ crystals show two major emission bands, with the first band peaking at 494 nm and the second centered around 568 nm (Figure 2b). The associated average PL lifetimes are 23.27 and 19.06 ms, respectively (Figure 2c, d). Time-resolved emission spectra

showed a similar emission profile as the steady-state spectrum (Figure 2b). The collected time-gated PL spectra at various delay times revealed that the 494 nm emission band has a slower decay process than the 568 nm emission band (Figure 2e), consistent with the result of lifetime measurements. The nanosecond-scale component observed in the decay profile of the 494 nm emission is associated with prompt fluorescence (Figure S11).[11] Therefore, the emission at 494 nm is attributed to a combination of prompt fluorescence and TADF, while the 568 nm emission is due to phosphorescence from the triplet state (Figure S12). The bi-exponential decay observed at 568 nm results from the combined effects of hybrid charge-transfer and locally excited components. To further validate this interpretation, the phosphorescence lifetime was measured at 660 nm, a wavelength at which singlet state emission does not occur. This was supported by the time-resolved photoluminescence decay curve at 660 nm, which agrees well with a bi-exponential model similar to that at 568 nm (Figure S13). In addition, these findings were corroborated through calculations.

To shed light on the luminescence centers of $TpyBiCl_5$, the photophysical properties of the individual Tpy were also investigated. The steady-state PL spectrum reveals that Tpy shows a broad and structured emission band with peak maxima at 438, 462, 494, and 529 nm (Figure 2f). The red-shifted emission band at 494 nm compared to that of Tpy is the result of electronic coupling between the organic and inorganic components. The time-gated PL spectrum detected long-lived phosphorescence emission, centered at 568 and 617 nm (Figure 2f), which is consistent with the previous report.[10] There is no observable emission of metal halide

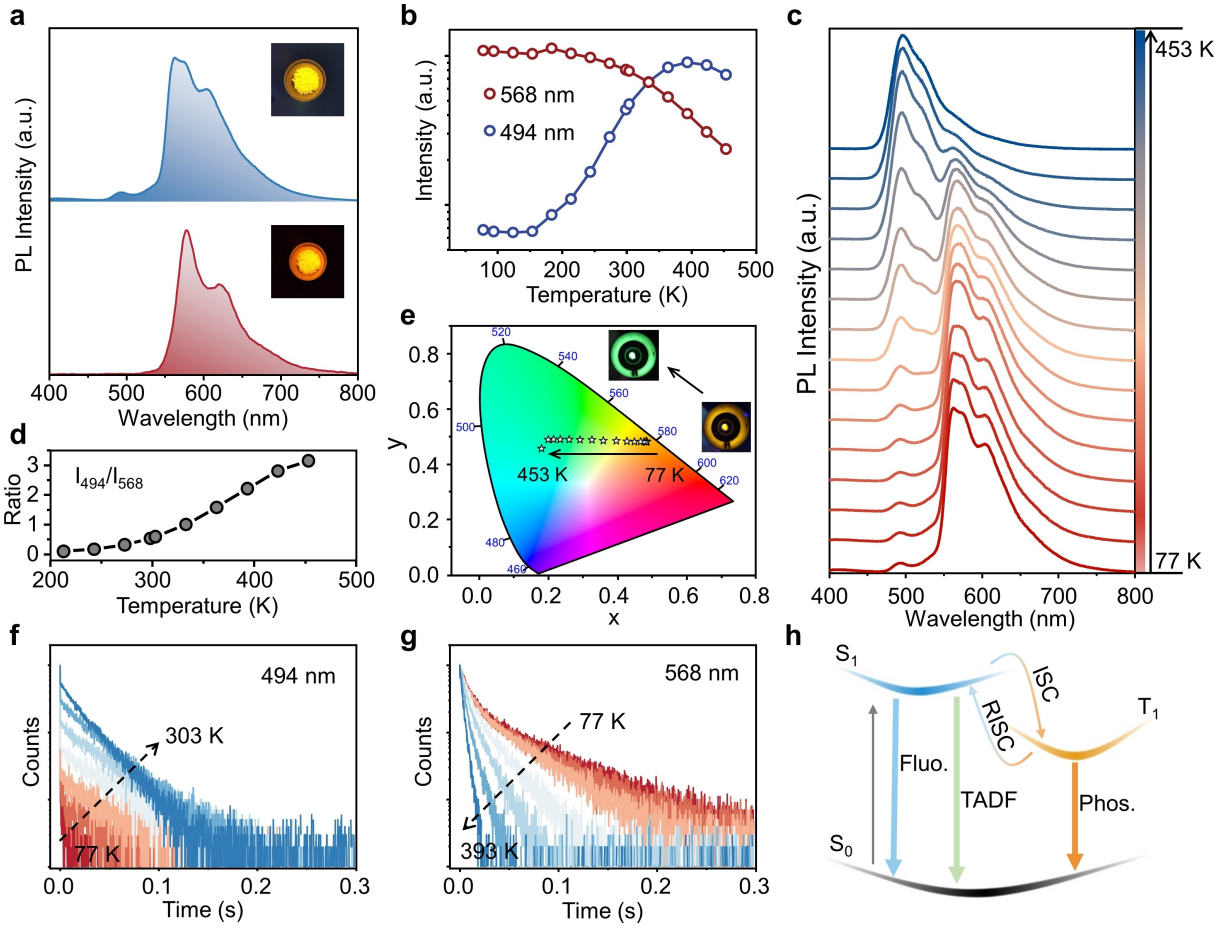

Figure 3. (a) Steady-state (blue) and time-gated PL spectra (red) of $TpyBiCl_5$ at 77 K ($\lambda_{ex}=360$ nm). Insets: photographs of $TpyBiCl_5$ crystals taken before and after turning off the ultraviolet lamp (395 nm) at 77 K. (b) Emission intensity of $TpyBiCl_5$ at 494 nm (blue) and 568 nm (red) as a function of temperature (77–453 K). These two emission bands show an opposite trend with temperature changes. (c) PL spectra of $TpyBiCl_5$ were recorded at different temperatures ranging from 77–453 K. At low temperatures, the spectrum consists mainly of the 568 nm emission band, while 494 nm is the dormant emission at high temperatures. (d) Ratio of the intensity of two emission bands (I_{494}/I_{568}) as a function of temperature (77–453 K). (e) Evolution of the CIE coordinates of $TpyBiCl_5$ at different temperatures. The black arrow indicates the direction of the temperature increase. Insets: photographs of $TpyBiCl_5$ taken at 77 K (yellow) and 453 K (green) ($\lambda_{ex}=360$ nm). (f) and (g), Temperature-dependent time-resolved PL decay profiles of $TpyBiCl_5$ at (f) 494 nm recorded from 77 K to 303 K and (g) 568 nm recorded from 77 K to 393 K ($\lambda_{ex}=360$ nm). (h) Mechanistic illustration of the tri-mode emission of $TpyBiCl_5$ using a simplified Jablonski diagram. Prompt fluorescence, thermally activated delayed fluorescence, phosphorescence, intersystem crossing, and reverse intersystem crossing are abbreviated as Fluo., TADF, Phos., ISC and RISC, respectively.

$BiCl_3$ from 400 nm to 800 nm (Figure S14). These results indicate that the phosphorescence of $TpyBiCl_5$ is mainly dominated by its organic unit (Tpy). Moreover, no phosphorescence peak shift was observed with the change of excitation wavelength (Figure 2g), suggesting that no other impurities contribute to the phosphorescence of $TpyBiCl_5$.[12] The presence of hydrogen bonds (N–H···Cl) between Tpy and halides creates a rigid environment that suppresses the non-radiative relaxation of triplet excitons (Figure S15), evidenced by an increase in room-temperature phosphorescence quantum yield from 3.8 % to 45 % (Figure 2h and Table S3). Meanwhile, the phosphorescence lifetime of Tpy decreases from 165.25 to 19.06 ms (Figure S16) because the abundant heavy atoms accelerate the forbidden $T_1 \rightarrow S_0$ transition.

To further elucidate the luminescence mechanism of $TpyBiCl_5$, temperature-dependent PL measurement was performed. At 77 K, the phosphorescence emission of $TpyBiCl_5$ completely prevails over TADF in both steady-state and time-gated spectra due to the suppressed thermal quenching (Figure 3a). As temperature increases, the PL of $TpyBiCl_5$ gradually evolves into the regime dominated by TADF, resulting from thermal activation, which consequently consumes triplet excitons and thus weakens the phosphorescence emission (Figure 3b, c). The monotonically increasing emission intensity ratio between 494 nm and 568 nm (I_{494}/I_{568}) over temperature indicates the thermally activated RISC process (Figure 3d). As reflected by the Commission Internationale de l'éclairage (CIE) diagram, the PL color changes from yellow (phosphorescence) to green (TADF) as temperatures increase from 77 to 453 K (Figure 3e). The variation trend of PL lifetime as temperature increases further demonstrates that the 494 and 568 nm emission bands are contributed by TADF and phosphorescence (Figure 3f, g and Figure S17), respectively. Thus, we can rationally conclude that tri-mode PL consists of prompt fluorescence, TADF, and phosphorescence (Figure 3h).

Furthermore, we conducted the density functional (DFT) theory calculation using the Vienna ab initio Simulation Package (VASP) at the generalized gradient approximation (GGA) level to reveal the emission contributions of components from a theoretical perspective. As shown in Figure 4a, $TpyBiCl_5$ has a direct band gap, which contributes to its high PL quantum yield of 60.76 % (Figure S18). The calculated band gap of 2.0 eV is close to that obtained from the UV/Vis absorption edge (1.97 eV) (Figure S19). The total and partial density of states of $TpyBiCl_5$ perovskite show a $[Bi_2Cl_{10}]^{4-}$-derived valence band and a Tpy-derived conduction band (Figure 4b). Furthermore, the wavefunctions of the highest occupied molecular orbital (HOMO) and lowest unoccupied molecular orbital

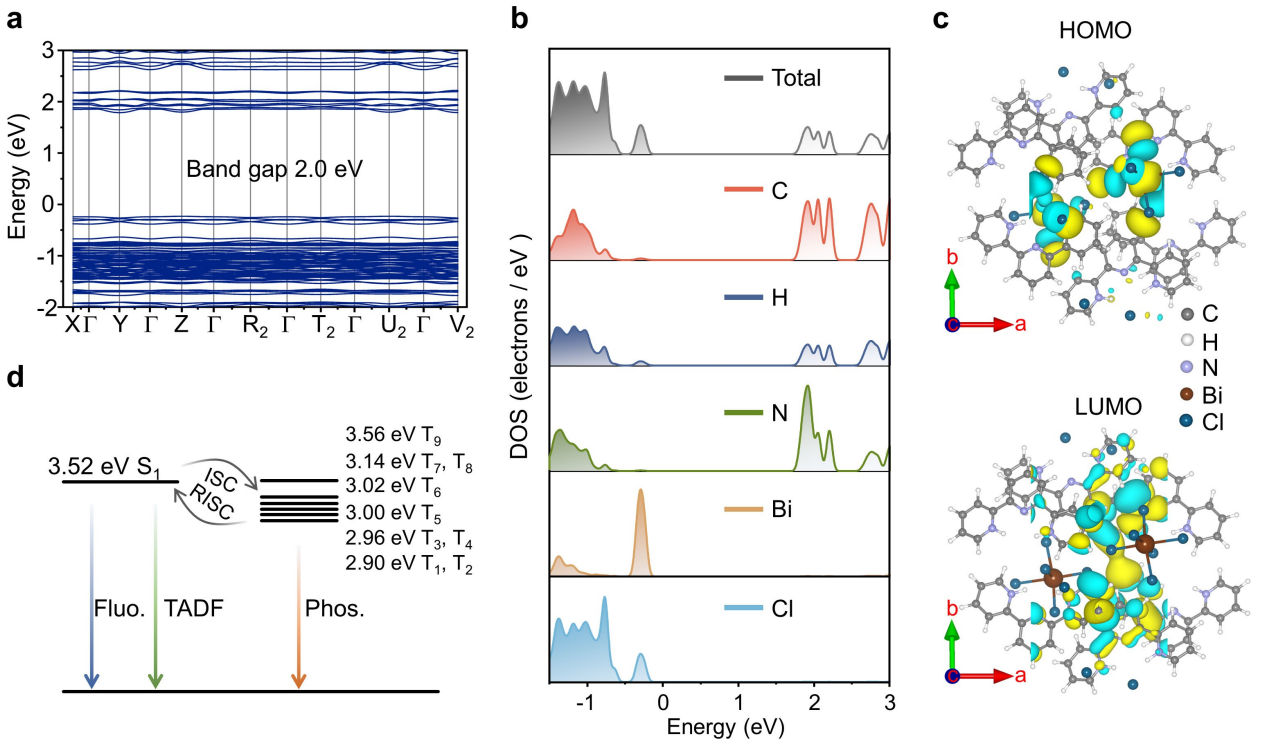

Figure 4. (a) Calculated band structure of $TpyBiCl_5$. The calculated band gap value is 2.0 eV, which is consistent with the experimental results. (b) Total and partial density of states (DOS) of $TpyBiCl_5$. The conduction band consists mainly of C, H and N elements, while the valence band consists mainly of Bi and Cl elements. (c) Real-space wave functions of the highest occupied molecular orbital (HOMO) and the lowest unoccupied molecular orbital (LUMO) with an isosurface of 2×10^{-8} e $Bohr^{-3}$. (d) Calculated energy level diagram of $TpyBiCl_5$ (vertical excitation). There are eight triplet states (T_1–T_8) below the S_1 state and the smallest energy gap between them is 0.38 eV. All results were calculated in single crystals; (a–c) were calculated using the Vienna ab initio Simulation Package (VASP) at the generalized gradient approximation (GGA) level; (d) was calculated using the hybrid functional PBE0 in conjunction with the TZVP-MOLOPT-GTH basis set and GTH-PBE potential.

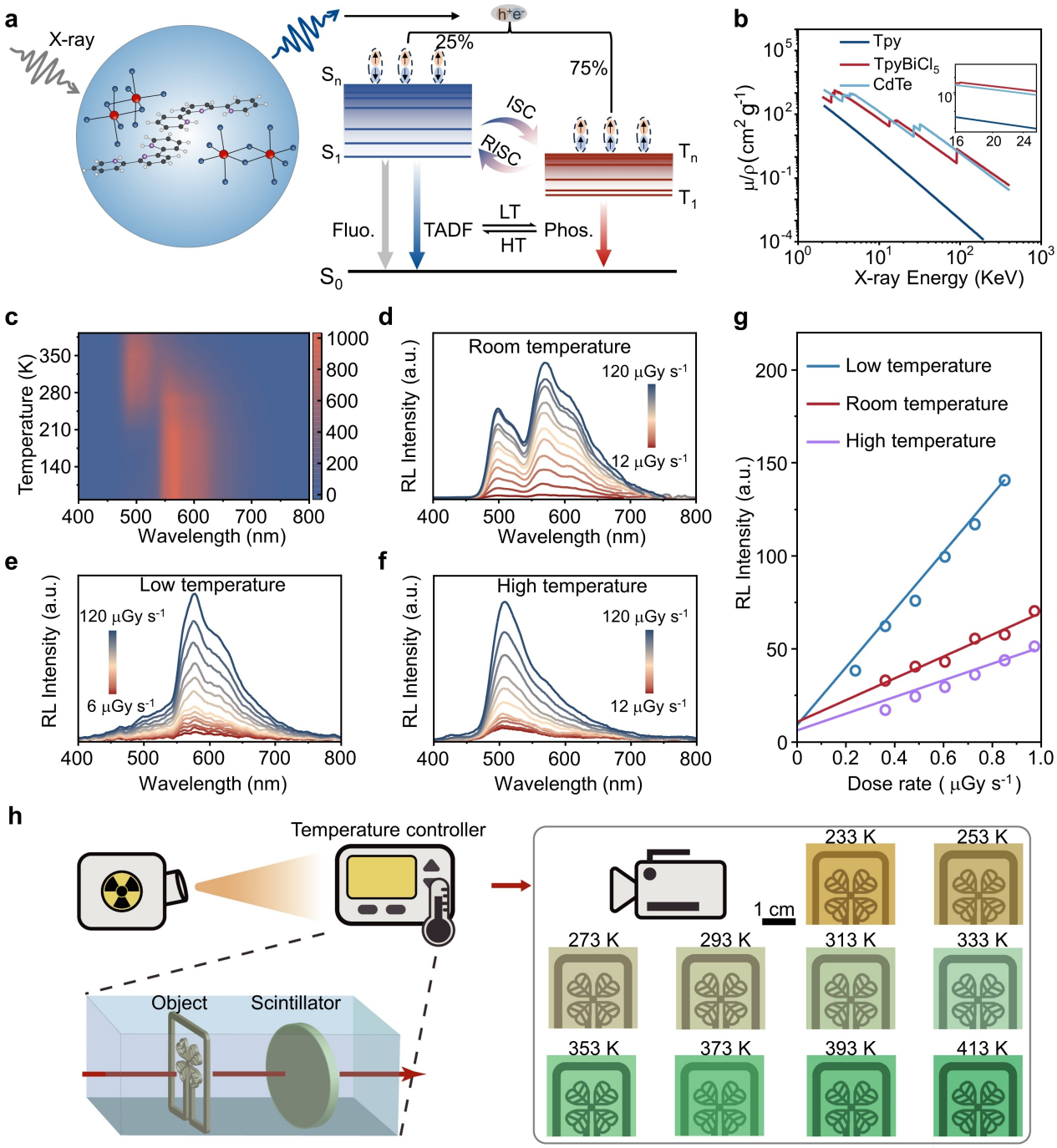

Figure 5. (a) Radioluminescence mechanism of $TpyBiCl_5$ at varied temperatures under X-ray irradiation. Under X-ray irradiation, the single and triplet excitons are generated in a ratio of 1 : 3 according to the rule of spin conservation. For $TpyBiCl_5$, there is a dynamical thermal equilibrium between singlet and triplet. At room temperature, prompt fluorescence, thermally activated delayed fluorescence (TADF), and room-temperature phosphorescence emission contribute to radioluminescence. With increasing temperature, the TADF mode is the main radioluminescence mode by the RISC process. Instead, the dominant radioluminescence mode is converted to phosphorescence by the ISC process at low temperatures. (b) Absorption spectra of CdTe, Tpy, and $TpyBiCl_5$ as a function of X-ray energy. (c) Temperature-dependent radioluminescence spectra of $TpyBiCl_5$ under X-rays (77 K to 393 K). (d–f) Dose-rate-dependent radioluminescence spectra of $TpyBiCl_5$ at room temperature (298 K), low temperature (213 K), and high temperature (353 K). (g) X-ray detection limits and linear behaviour of $TpyBiCl_5$ at different temperatures. The detection limits can be defined as the dose rate at which the signal-to-noise ratio equals 3. (h) Left: schematic of the temperature-dependent X-ray imaging system, where the object and the scintillator ($TpyBiCl_5$@PDMS film) are placed inside a temperature controller. Right: X-ray images of a metal bookmark showing that the image colors vary with temperature from 233 K to 413 K.

(LUMO) are localized on the metal halide $[Bi_2Cl_{10}]^{4-}$ and the organic unit Tpy, respectively (Figure 4c). These results provide evidence of charge transfer between organic and inorganic components, which plays a significant role in TADF. This observation also supports the determination of the decay lifetime at 568 nm (Figure S13). The calculated vertical excitation energies reveal the smallest energy gap between the singlet and triplet states to be 0.38 eV (Figure 4d), which closely aligns with the experimental result ($\Delta_{ST} = 0.35$ eV, estimated from the onset of fluorescence and phosphorescence emissions, Figure S20). This relatively big Δ_{ST} explains why TADF possesses a millisecond radiative emission. Besides, the multiple triplet excited states(T_1–T_8) can serve as receiver states for producing triplet exciton to improve the phosphorescence efficiency. For Tpy, all the calculated T_1–T_{15} states are below the S_1 state and the Δ_{ST} is 0.72 eV, which is consistent with the experimental result (Figure S20–21). Thus, the smaller Δ_{ST}, heavy atoms, and organic–inorganic electronic coupling in $TpyBiCl_5$ explain the concurrence of prompt fluorescence, TADF, and phosphorescence.

Different from UV excitation, incident X-ray photons interact with high Z atoms in the scintillator, producing a large number of hot electrons and holes through the photoelectric effect. After thermalization of hot carriers, the produced low-energy holes and electrons recombine into 25 % singlet and 75 % triplet excitons, associated with ISC and RISC for TADF and phosphorescence (Figure 5a and Figure S22).[2b,5a] Compared to conventional fluorescence scintillators, higher exciton utilization efficiency can be achieved in $TpyBiCl_5$ benefitting from simultaneous tri-mode emission channels. The absorption coefficient of $TpyBiCl_5$ crystal is comparable to that of commercial CdTe and even exceeds it in the energy range of 16–26 KeV (Figure 5b). Heavy atoms of Bi and Cl, endow $TpyBiCl_5$ with a much higher X-ray absorption coefficient (increases exponentially with the effective atomic number) than individual Tpy molecule.

The temperature-dependent radioluminescence spectra of $TpyBiCl_5$ exhibit a similar trend to its temperature-dependent PL spectra (Figure 5c). In addition, the radioluminescence intensity of $TpyBiCl_5$ is linearly correlated with the dose rate of the X-ray source at specific temperatures (Figure 5d–f). Accordingly, the detection limits for this material are 38.92 at 213 K, 73.04 at 298 K and 196.31 $nGy\,s^{-1}$ at 353 K (Figure 5g). These values are approximately 141, 75, and 28 times lower than that required for conventional medical X-ray diagnosis (5.5 $\mu Gy_{air}\,s^{-1}$).[13] $TpyBiCl_5$ also exhibits excellent performance in temperature-dependent X-ray imaging. Notably, the color of the X-ray images shifts from yellow to green when the temperature rises from 233 K to 413 K, which is consistent with the temperature-dependent radioluminescence (Figure 5h). The materials' thermally activated radioluminescence channel enables high-resolution imaging at 413 K. This effectively solves the problem of thermal quenching that often occurs with other materials. This high-resolution imaging makes it possible to observe intricate details, such as the internal configuration of electronic chips, circuit board lines, and encapsulated metal springs, with the naked eye (Figure S23–24). Although traditional luminescent materials also respond to temperature changes, their application at high temperatures is often limited due to thermal quenching, a problem often encountered with organic scintillators based on phosphorescence. Moreover, the mere existence of temperature-sensitive materials is no guarantee of effective scintillation.[14] In contrast, the unique X-ray scintillation performance of $TpyBiCl_5$ perovskites at elevated temperatures is achieved by alternating the scintillation mode between TADF and phosphorescence.

In summary, we have reported a zero-dimension hybrid perovskite scintillator with tri-mode emission (prompt fluorescence, TADF, and phosphorescence), which mitigates thermal quenching through dynamically switching between different excited states. Photophysical and theoretical investigations demonstrate that TADF originates from the electron coupling between organic and inorganic components, while phosphorescence is dominated by the organic subunit Tpy. Benefitting from the synergy of rigid framework and enhanced spin-orbit coupling of the constructed perovskite, the room-temperature phosphorescence quantum yield improves from 3.8 % to 45 %. Remarkable temperature responsiveness was evidenced by the temperature-dependent PL study by monitoring the evolution of TADF and phosphorescence emissions. Due to prominent temperature-responsive multi-mode emission, X-ray scintillation using $TpyBiCl_5$ behaved with a desirable performance (detection limit = 73.04 $nGy\,s^{-1}$) at room temperature. The detection limit is 38.92 $nGy\,s^{-1}$ at low temperature (213 K, phosphorescence mode), which surprisingly remains at 196.31 $nGy\,s^{-1}$ at high temperature (353 K, TADF mode). This work advances the research of hybrid perovskites, which will provide new insights for the designation of efficient scintillators worked in abnormal environments.

Acknowledgements

The authors acknowledge the support from National Research Foundation, Prime Minister's Office, Singapore under its Competitive Research Program (Award No. NRF-CRP23-2019-0002). Computational work was performed with high-performance computing facilities in NUS High Performance Computing (HPC) center, A*STAR Computational Resource Centre (ACRC) and National Supercomputing Centre (NSCC) in Singapore. The authors are grateful to Prof. Chuang Zhang at Institute of Chemistry Chinese Academy of Science.

Conflict of Interest

The authors declare no conflict of interest.

Data Availability Statement

The data that support the findings of this study are available from the corresponding author upon reasonable request.

Keywords: Scintillator · Thermal Quenching · Hybrid Perovskites · Multi-Excited State Switching

[1] a) M. Yaffe, J. Rowlands, *Phys. Med. Biol.* **1997**, *42*, 1; b) L. Yi, B. Hou, H. Zhao, X. Liu, *Nature* **2023**, *618*, 281–286; c) F. Moretti, G. Patton, A. Belsky, M. Fasoli, A. Vedda, M. Trevisani, M. Bettinelli, C. Dujardin, *J. Phys. Chem. C* **2014**, *118*, 9670–9676; d) P. Büchele, M. Richter, S. F. Tedde, G. J. Matt, G. N. Ankah, R. Fischer, M. Biele, W. Metzger, S. Lilliu, O. Bikondoa, *Nat. Photonics* **2015**, *9*, 843–848; e) T. Jin, Z. Liu, J. Luo, J.-H. Yuan, H. Wang, Z. Xie, W. Pan, H. Wu, K.-H. Xue, L. Liu, Z. Hu, Z. Zheng, J. Tang, G. Niu, *Nat. Commun.* **2023**, *14*, 2808; f) H. Wei, J. Huang, *Nat. Commun.* **2019**, *10*, 1066.

[2] a) V. Nagarkar, T. Gupta, S. Miller, Y. Klugerman, M. Squillante, G. Entine, *IEEE Trans. Nucl. Sci.* **1998**, *45*, 492–496; b) Q. Chen, J. Wu, X. Ou, B. Huang, J. Almutlaq, A. A. Zhumekenov, X. Guan, S. Han, L. Liang, Z. Yi, J. Li, X. Xie, Y. Wang, Y. Li, D. Fan, D. B. L. Teh, A. H. All, O. F. Mohammed, O. M. Bakr, T. Wu, M. Bettinelli, H. Yang, W. Huang, X. Liu, *Nature* **2018**, *561*, 88–93; c) H. Zhao, J. Qiu, B. Hou, L. Yi, X. Qin, X. Liu, *Adv. Opt. Mater.* **2023**, *11*, 2202668.

[3] a) Y. Cui, R. Song, J. Yu, M. Liu, Z. Wang, C. Wu, Y. Yang, Z. Wang, B. Chen, G. Qian, *Adv. Mater.* **2015**, *27*, 1420–1425; b) M. Kong, Y. Gu, Y. Chai, J. Ke, Y. Liu, X. Xu, Z. Li, W. Feng, F. Li, *Sci. China Chem.* **2021**, *64*, 974–984; c) E. Song, M. Chen, Z. Chen, Y. Zhou, W. Zhou, H.-T. Sun, X. Yang, J. Gan, S. Ye, Q. Zhang, *Nat. Commun.* **2022**, *13*, 2166.

[4] a) T. Wang, A. K. Gupta, S. Wu, A. M. Z. Slawin, E. Zysman-Colman, *J. Am. Chem. Soc.* **2023**, *145*, 1945–1954; b) T. Wang, J. De, S. Wu, A. K. Gupta, E. Zysman-Colman, *Angew. Chem. Int. Ed.* **2022**, *61*, e202206681; c) C. Chen, R. Huang, A. S. Batsanov, P. Pander, Y.-T. Hsu, Z. Chi, F. B. Dias, M. R. Bryce, *Angew. Chem. Int. Ed.* **2018**, *57*, 16407–16411.

[5] a) W. Ma, Y. Su, Q. Zhang, C. Deng, L. Pasquali, W. Zhu, Y. Tian, P. Ran, Z. Chen, G. Yang, G. Liang, T. Liu, H. Zhu, P. Huang, H. Zhong, K. Wang, S. Peng, J. Xia, H. Liu, X. Liu, Y. M. Yang, *Nat. Mater.* **2022**, *21*, 210–216; b) J.-X. Wang, L. Gutiérrez-Arzaluz, X. Wang, T. He, Y. Zhang, M. Eddaoudi, O. M. Bakr, O. F. Mohammed, *Nat. Photonics* **2022**, *16*, 869–875; c) X. Wang, H. Shi, H. Ma, W. Ye, L. Song, J. Zan, X. Yao, X. Ou, G. Yang, Z. Zhao, M. Singh, C. Lin, H. Wang, W. Jia, Q. Wang, J. Zhi, C. Dong, X. Jiang, Y. Tang, X. Xie, Y. Yang, J. Wang, Q. Chen, Y. Wang, H. Yang, G. Zhang, Z. An, X. Liu, W. Huang, *Nat. Photonics* **2021**, *15*, 187–192; d) W.-F. Wang, M.-J. Xie, P.-K. Wang, J. Lu, B.-Y. Li, M.-S. Wang, S.-H. Wang, F.-K. Zheng, G.-C. Guo, *Angew. Chem. Int. Ed.* e202318026. 10.1002/anie.202318026.

[6] a) J. Jin, H. Jiang, Q. Yang, L. Tang, Y. Tao, Y. Li, R. Chen, C. Zheng, Q. Fan, K. Y. Zhang, Q. Zhao, W. Huang, *Nat. Commun.* **2020**, *11*, 842; b) J. Wang, X. Gu, H. Ma, Q. Peng, X. Huang, X. Zheng, S. H. P. Sung, G. Shan, J. W. Y. Lam, Z. Shuai, B. Z. Tang, *Nat. Commun.* **2018**, *9*, 2963; c) M. Li, W. Xie, X. Cai, X. Peng, K. Liu, Q. Gu, J. Zhou, W. Qiu, Z. Chen, Y. Gan, S. J. Su, *Angew. Chem. Int. Ed.* **2022**, *61*, e202209343.

[7] a) M. Wang, J. Tang, H. Wang, C. Zhang, Y. S. Zhao, J. Yao, *Adv. Opt. Mater.* **2020**, *8*, 1901780; b) Y. Zhang, Y. Zhang, Y. Zhao, H. Jia, Z. Yang, B. Yin, Y. Wu, Y. Yi, C. Zhang, J. Yao, *J. Am. Chem. Soc.* **2023**, *145*, 12360–12369; c) B. Zhou, D. Yan, *Angew. Chem. Int. Ed.* **2019**, *58*, 15128–15135; d) R. Zhang, X. Mao, Y. Yang, S. Yang, W. Zhao, T. Wumaier, D. Wei, W. Deng, K. Han, *Angew. Chem. Int. Ed.* **2019**, *58*, 2725–2729; e) J. H. Wei, W. T. Ou, J. B. Luo, D. B. Kuang, *Angew. Chem. Int. Ed.* **2022**, *134*, e202207985; f) L. J. Xu, X. Lin, Q. He, M. Worku, B. Ma, *Nat. Commun.* **2020**, *11*, 4329.

[8] a) L. Zhan, Z. Chen, S. Gong, Y. Xiang, F. Ni, X. Zeng, G. Xie, C. Yang, *Angew. Chem. Int. Ed.* **2019**, *131*, 17815–17819; b) N. Zhang, L. Qu, S. Dai, G. Xie, C. Han, J. Zhang, R. Huo, H. Hu, Q. Chen, W. Huang, H. Xu, *Nat. Commun.* **2023**, *14*, 2901.

[9] a) C. Han, R. Du, H. Xu, S. Han, P. Ma, J. Bian, C. Duan, Y. Wei, M. Sun, X. Liu, W. Huang, *Nat. Commun.* **2021**, *12*, 3640; b) J.-K. Chen, N. Shirahata, H.-T. Sun, *Nat. Photonics* **2021**, *15*, 171–172.

[10] A. Sarkar, S. Chakravorti, *J. Lumin.* **1995**, *63*, 143–148.

[11] J. Wang, Y. Yang, K. Li, L. Zhang, Z. Li, *Angew. Chem. Int. Ed.* **2023**, e202304020.

[12] H. Gong, H. Yu, Y. Zhang, L. Feng, Y. Tian, G. Cui, H. Fu, *Angew. Chem. Int. Ed.* **2023**, *135*, e202219085.

[13] D. R. Shearer, M. Bopaiah, *Health Phys.* **2000**, *79*, S20–S21.

[14] W. Dai, X. Niu, X. Wu, Y. Ren, Y. Zhang, G. Li, H. Su, Y. Lei, J. Xiao, J. Shi, B. Tong, Z. Cai, Y. Dong, *Angew. Chem. Int. Ed.* **2022**, *61*, e202200236.

Manuscript received: January 28, 2024
Accepted manuscript online: March 4, 2024
Version of record online: March 21, 2024